The American Journal of Pathology, Vol. 184, No. 11, November 2014

The American Journal of
PATHOLOGY
ajp.amjpathol.org

CELL INJURY, REPAIR, AGING, AND APOPTOSIS

WFDC1 Is a Key Modulator of Inflammatory and Wound Repair Responses

Steven J. Ressler,* Truong D. Dang,* Samuel M. Wu,† Dennis Y. Tse,† Brian E. Gilbert,‡ Annapurna Vyakarnam,§ Feng Yang,* Isaiah G. Schauer,* David A. Barron,* and David R. Rowley*

From the Departments of Molecular and Cellular Biology, Ophthalmology,† and Molecular Virology and Microbiology,‡ Baylor College of Medicine, Houston, Texas; and the Department of Infectious Diseases,§ King's College London, London, United Kingdom*

Accepted for publication July 24, 2014.

Address correspondence to David R. Rowley, Ph.D., 1 Baylor Plaza Baylor College of Medicine Houston, TX 77030. E-mail: drowley@bcm.edu.

WFDC1/ps20 is a whey acidic protein four-disulfide core member that exhibits diverse growth and immune-associated functions *in vitro*. *In vivo* functions are unknown, although WFDC1 is lower in reactive stroma. A *Wfdc1*-null mouse was generated to assess core functions. *Wfdc1*-null mice exhibited normal developmental and adult phenotypes. However, homeostasis challenges affected inflammatory and repair processes. *Wfdc1*-null mice infected with influenza A exhibited 2.75—log-fold lower viral titer relative to control mice. *Wfdc1*-null infected lungs exhibited elevated macrophages and deposition of osteopontin, a potent macrophage chemokine. In wounding studies, *Wfdc1*-null mice exhibited an elevated rate of skin closure, and this too was associated with elevated deposition of osteopontin and macrophage recruitment. *Wfdc1*-null fibroblasts exhibited impaired spheroid formation, elevated adhesion to fibronectin, and an increased rate of wound closure *in vitro*. This was reversed by neutralizing antibody to osteopontin. Osteopontin mRNA and cleaved protein was up-regulated in *Wfdc1*-null cells treated with lipopolysaccharide or polyinosinic-polycytidylic acid coordinate with constitutively active matrix metallopeptidase-9 (MMP-9), a protease that cleaves osteopontin. These data suggest that WFDC1/ps20 modulates core host response mechanisms, in part, via regulation of osteopontin and MMP-9 activity. Release from WFDC1 regulation is likely a key component of inflammatory and repair response mechanisms, and involves the processing of elevated osteopontin by activated MMP-9, and subsequent macrophage recruitment. *(Am J Pathol 2014, 184: 2951—2964; http://dx.doi.org/10.1016/j.ajpath.2014.07.013)*

We have previously reported the growth inhibitory functions of ps20 *in vitro*,[1,2] purified the secreted ps20 protein,[3] and cloned the rodent and human *WFDC1* genes encoding ps20.[4,5] Rodent and human mRNA encoding ps20 are highly conserved, exhibit a canonical four-disulfide core domain typical of the whey acidic protein (WAP) family, and localize to human chromosome 16q24.[4,5] By contrast, many of the other WAP family members are clustered on chromosome 20q13, suggesting *WFDC1* had a divergent evolutionary origin.[4,6] Eighteen human WAP proteins have been identified; most are secreted factors that exhibit protease inhibitory activity and contain at least one canonical four-disulfide core domain.[7] The WAP family members exhibit several diverse biological functions associated with immune responses and antimicrobial activity.[6] However, the biology and function of WFDC1/ps20 *in vivo* is poorly understood.

Several *in vitro* studies suggested WFDC1/ps20 functions in stromal—epithelial interactions and tissue homeostasis.[1—3] Further study showed that WFDC1/ps20 expression was reduced in reactive stroma in human prostate cancer, and this was predictive of prostate cancer progression.[8] Reactive stroma in cancer is very similar to wound repair reactive stroma generally observed at sites of altered tissue homeostasis,

Supported by NIH grants R01 CA58093 and R01 DK083293 (D.R.R.); NCI Cancer Center Support grant P30 CA125123 (the Dan L. Duncan Cancer Center at Baylor College of Medicine); and the Genetically Engineered Mouse (GEM) Shared Resource (Baylor College of Medicine).

The funders had no role in the study design, data collection and analysis, decision to publish, or preparation of the manuscript.

Disclosures: None declared.

Current address of S.J.R., Aptalis Pharmaceuticals, Bridgewater, NJ; of I.G.S., Department of Mathematics and Life Sciences, Brazosport College, Lake Jackson, TX; and of D.A.B., Department of Radiation Oncology, Memorial Sloan-Kettering Cancer Center, New York, NY.

http://dx.doi.org/10.1016/j.ajpath.2014.07.013

including wound repair, fibrosis, cancer, and cardiovascular disease.[9–11] Conversely, *in vivo* studies showed that overexpression of WFDC1/ps20 in a recombined cancer/stromal cell mixed xenograft model resulted in elevated tumorigenesis attributable to elevated angiogenesis.[12] Together, these studies suggest that WFDC1/ps20 functions in adult tissue homeostasis by modulating cell proliferation, adhesion, and migration.

Additional studies support the notion that WFDC1/ps20 functions during infection processes and immune responses. Human WFDC1/ps20 promoted HIV infection in CD4 T cells by up-regulating intercellular adhesion molecule 1,[13] whereas murine *Wfdc1* limited murine hepatitis virus infectivity and neutrophil recruitment[14] in our mouse model, suggesting differential innate immune functions. Other studies have shown that mutations in WFDC1 were associated with macular degeneration leading to blindness,[15–17] although mechanisms were not addressed.

In summary, previous studies suggest that WFDC1/ps20 may function as a regulator of diverse cell responses associated with general homeostasis involving tissue repair and immunity. To evaluate *in vivo* functions and address the hypothesis directly, we generated a *Wfdc1*-null mouse to assess the null phenotype and to pinpoint changes in host response mechanisms during homeostasis challenges. We report here that *Wfdc1*-null mice challenged with viral infection or physical wounding exhibit clear biological alterations. *Wfdc1*-null mice exhibited marked resistance to influenza virus infection and more robust wound repair responses with elevated and earlier recruitment of macrophages. These homeostasis responses were associated with elevated *Spp1*/osteopontin and constitutively active matrix metallopeptidase-9 (MMP-9) that mediated some of *Wfdc1*-null associated biology. Together, these data suggest that *Wfdc1* represses emergency response mechanisms during resting, normal adult tissue homeostasis and that release from *Wfdc1* regulation at sites of reactive and repair tissue biology is a key permissive event in coordination of core inflammatory and repair processes.

Materials and Methods

Wfdc1 Knockout/Knockin Mouse

A *Wfdc1*-null mouse was generated via knockout of exon 1 and insertion of *lac*Z inframe with the *Wfdc1* ATG start codon. The 5′ homology arm using the *Wfdc1* genomic clone AF169632.1 was digested with SpeI, resulting in a fragment containing nucleotides −2542 to +418 (relative to the ATG) (that includes exon 1) cloned into an SpeI site in pSK- (Stratagene, Santa Clara, CA). An NcoI sense primer 5′-GCCACCAGCCTCGCCATGGGTAACTGCG-3′ (NcoI site underlined) along with the anti-sense complement was used in the Stratagene QuikChange Mutagenesis Kit to mutate the *Wfdc1* ATG to an NcoI site to generate the construct pSpeINcoImutant. We then mutated the *lac*Z ATG to an NcoI site in the construct pPD46.21, obtained from Dr. Franco DeMayo [Baylor College of Medicine (BCM)], that contains a 3.3-kb *lac*Z fragment with an SV40 nuclear localization site. A *lac*Z sense primer 5′-CCGAGCTCA-GAAACCATGGCTGCTCCAAAGAAGAAGCG-3′ (NcoI site underlined) along with the anti-sense complement was used in the Stratagene QuikChange Mutagenesis Kit to mutate the ATG from *lacZ* start to an NcoI site to generate pPD46.21NcoImutant. The NcoI mutant constructs were digested with NcoI and SalI, and the 3.3-kb *lacZ* NcoI mutant fragment cloned into the pSpeINcoImutant construct at the *Wfdc1* ATG site to produce pSpeIßgal that contains −2542 to +1 of *Wfdc1* and a 3.3-kb *lacZ* gene. To generate a 3′ homology arm using a XhoI to ApaI digest of MGL5-II1S4, a *Wfdc1* genomic clone containing exon 1 and part of intron 1, which generates a fragment from +549 to +3883, was used. This 3334-bp 3′ homology arm was cloned in a 3-way ligation with the 5′ homology arm from the pSpeIßgal construct that was digested with ApaI and XhoI to generate a fragment containing +1170 to +1 of the *Wfdc1* promoter with the 3.3-kb *lacZ* gene and a 1.7-kb XhoI fragment from PGKNeo that contains the phosphoglycerate kinase (PGK) promoter and neo gene cassette. All three fragments were cloned into pSK- that was linearized with ApaI to generate the *Wfdc1*KO/KI construct. The orientation of the PGK-neo cassette was cloned in the antisense direction relative to the *lacZ* gene. The *Wfdc1*KO/KI construct was sequenced to verify position and orientation. The *Wfdc1*KO/KI construct was then linearized with ApaI and injected into AB2.2 p.13 embryonic stem cells by the GEM core at BCM.

Chimeric mice were mated to C57Bl/6 mice for four to five generations and given the name *Wfdc1*^{tm1LaczBCM}. Use of mice was carried out according to the Animal Welfare Act, PHS Animal Welfare Policy, the principles of the NIH Guide for the Care and Use of Laboratory Animals,[18] and the policies of BCM.

Screening *Wfdc1* Knockout Mice

The *Wfdc1* knockout/knockin (KO/KI) mice were screened by Southern blotting using a 1.3-kb probe spanning nucleotides +2542 (SpeI) to +1170 (ApaI). The introduction of the *lacZ* gene produced an extra EcoRV site that on digestion of the genomic DNA with EcoRV and hybridization with the 1.3-kb SpeI-ApaI probe yielded a 6.5-kb knockout allele and a 9.5-kb wild-type allele. Subsequently, mice were screened by PCR using two reactions each containing primers to mouse β-actin and either primers to *Wfdc1*exon1 sense (5′-GGAGGTCACTCGTGCA-3′) and *Wfdc1* antisense (5′-CAGCATTGCCTCCCAA-3′) or β-galactosidase (β-gal) sense (5′-TTCACTGGCCGTCGTTTTACAACG-TCGTGA-3′) and β-gal antisense (5′-ATGTGAGCGAG-TAACAACCCGTCGGATTCT-3′). Screening with the *Wfdc1*exon1 and β-gal primers yields 133-bp and 364-bp bands, respectively.

β-Gal Enzyme Staining of *Wfdc1*-Null Tissue

Tissues stained for β-gal enzyme were fixed in 4% paraformaldehyde for 1 to 2 hours, incubated in graduated 10% to 20% sucrose (in Hanks' balanced salt solution) over 3 days at 4°C, and then frozen in optimal cutting temperature compound. Frozen sections (10 μm) were postfixed in 0.2% glutaraldehyde, washed seven times in PBS (pH 8.3), and stained with X-Gal at 37°C overnight (O/N). Following staining for β-gal, some frozen tissues were also stained for CD34, Mac-3, and pro-SP-C.

Immunostaining after β-Gal Enzyme Staining

For immunostaining after β-gal enzyme staining, the tissue was evaluated for vessels using anti-mouse CD34 (#119301; BioLegend, San Diego, CA) at 1:100 dilution, for macrophages using anti-mouse Mac-3 (BD Pharmingen #553322; BD Biosciences, San Jose, CA) at 1:100 dilution, or for type II pneumocytes using anti-mouse pro-SP-C (WRAB-9337; Seven Hills Bioreagents, Cincinnati, OH) at 1:1600 dilution for 1 hour at room temperature. Streptavidin-AP followed by Vector Red substrate (Vector Laboratories, Burlingame, CA) was used to visualize the immunostaining. Images were acquired using a CRi multispectral deconvolution camera (N-MSI-420-FL) feeding a Macintosh Mac Pro computer (Apple, Cupertino, CA) running Nuance image analysis software version 3.0.0 (CRi, now PerkinElmer, Waltham, MA).

Immunostaining of Human Prostate

Human prostate sections were acquired from the Human Tissue Acquisition and Pathology Core Laboratory (Dan L. Duncan Cancer Center, BCM). An IgY antibody to a peptide (CVKQRRQADGRILRHKLYKEY) at amino acids 180 to 200 of the human ps20 protein was made by Aves Labs (Tigard, OR), tested for specificity, and used at 1:1200 dilution together with a rabbit anti-CD31 (#ab134168; Abcam, Cambridge, MA) at 1:400 dilution O/N at 4°C for colocalization of ps20 and CD31. Secondary antibodies [biotin-conjugated anti-chicken from Jackson ImmunoResearch Laboratories (West Grove, PA) #103-065-155 and the horseradish peroxidase (HRP)-conjugated goat anti-rabbit from Abcam #ab137913], were incubated for 45 minutes at 37°C. To develop the chicken anti-ps20 antibody, Streptavidin-AP (Vector Laboratories) was incubated (30 minutes at room temperature) followed by incubation with the Vector Blue substrate (Vector Laboratories) (30 minutes at room temperature). To develop the rabbit anti-CD31 antibody, the NovaRED substrate was incubated for 15 minutes at room temperature. Methyl Green (Vector Laboratories) was used as a counterstain. Images were converted to optical density (OD) and deconvoluted to separate blue (anti-ps20) from the red (anti-CD31) and green counterstain.

Electroretinogram

Four *Wfdc1*-heterozygous and four *Wfdc1*-null mice at 9 months of age for a total of eight eyes per group were tested for a blindness phenotype using an electroretinogram protocol as described previously.[19]

Influenza Virus Infections

Wild-type, heterozygous, and null *Wfdc1* KO/KI littermates (12 to 16 weeks of age) were anesthetized (with isoflurane), and 50 μL of approximately 10 median tissue culture infective doses of influenza A/Texas (H1N1) virus was inoculated intranasally. Mice were sacrificed at 4 days postinfection for infectivity assays and at days 7 and 14 to assess histopathology and immunohistochemistry (IHC). Lungs were harvested and lobes were frozen in 1 mL of minimal essential medium in tubes with glass beads, bead beaten, and then the supernatant collected for virus titering or fixed in 4% paraformaldehyde and embedded in paraffin for IHC.

Influenza Virus Titering

Round-bottom plates (96 well) were prepared with MDCK cells (CCL64; ATCC, Manassas, VA) 24 hours before titering. The medium was changed to 100 μL of minimal essential medium + Worthington Trypsin (0.5%) to prepare cells for viral infection. Frozen infected lungs were thawed and bead beaten for 60 seconds. The homogenate was centrifuged (5 minutes at 2000 × *g*), and a 1:10 dilution in minimal essential medium was made. Each mouse lung was titered in duplicate with a control. Diluted lung homogenate (50 μL) was added to 100 μL of medium, then serial dilutions (1:3) were performed across the plate and the plate incubated for 5 days at 37°C in 5% CO_2. Virus titer was determined by adding 50 to 100 μL of red blood cells/well and incubating for 30 minutes at room temperature. Statistical analysis of the virus titer comparing infected heterozygous versus null lungs was performed using an unpaired *t*-test with Welch's correction with the GraphPad Prism version 5 program (GraphPad Software, La Jolla, CA).

IHC of Influenza-Infected Tissue

IHC analysis of both uninfected and influenza-infected mouse tissues was performed as previously described[20,21] with modifications. Tissues were fixed in Zinc fixative (BD Pharmingen #550523; BD Biosciences) and processed for IHC without antigen retrieval to assess macrophage, osteopontin, and MMP-9 immunostaining. All secondary antibody incubations were at 37°C for 1 hour. To stain for macrophages, IHC was performed on tissue from wild-type, *Wfdc1*-heterozygous, and *Wfdc1*-null mice using rat monoclonal to macrophage (Abcam #ab56297) 1:500 dilution at 4°C O/N and with biotin-conjugated goat anti-rat IgG, (Invitrogen #D-20697; Life Technologies, Carlsbad, CA) 1:200 dilution.

To stain for MMP-9, IHC was performed on infected lung tissue from wild-type, *Wfdc1*-heterozygous, and null mice using rabbit anti-mouse MMP-9 (Abcam #ab38898) at 1:200 dilution at 4°C O/N and with biotin-conjugated goat anti-rabbit IgG, (Invitrogen #B-2770) at 1:500 dilution. To stain for osteopontin, IHC was performed on infected lung tissue from wild-type, *Wfdc1*-heterozygous, and null mice using goat anti-mouse osteopontin (#AF808; R&D Systems, Minneapolis, MN) at 1:400 dilution at 4°C O/N and with biotin-conjugated donkey anti-goat IgG, (Invitrogen #D-20698) at 1:500 dilution. Streptavidin-AP (Vector Laboratories #AK5000) and Vectastain Vector Red Substrate (Vector Laboratories #SK5100) were used to visualize staining.

Wfdc1 KO/KI Cell Lines

Stromal cells were isolated as reported previously.[1,22] Mouse lung, aorta, and prostate tissue were isolated from *Wfdc1*-heterozygous and null KO/KI mice, minced, and cultured in Bfs medium (DMEM; Gibco/Invitrogen) supplemented with 5% fetal bovine serum, 5% Nu Serum (BD Biosciences), 0.5 μg/mL testosterone, 5 μg/mL insulin, 100 U/mL penicillin, and 100 μg/mL streptomycin (Sigma-Aldrich, St. Louis, MO) in 24-well plates. At confluence, cells were passed 1:2 dilution and maintained in T25 flasks.

Spheroid Cultures and LPS or Poly I:C Treatment

For hanging-drop spheroid cultures, cells were trypsinized, centrifuged at 400 × *g* for 2 minutes, and resuspended in 8 mL of Bfs medium. Spots (25 to 30 20-μL spots) were made on the lid of a 100-mm^2 dish and cultured for 4 to 5 days. The spheroids were then collected and either plated onto a 100-mm^2 plate for β-gal expression analysis using X-Gal as a substrate or processed for RNA and subsequent gene expression analysis. For both lipopolysaccharide (LPS) and polyinosinic-polycytidylic acid (poly I:C) treatment, the *Wfdc1* KO/KI stromal heterozygous and null cells were plated onto 6-well plates and grown to 70% confluence. The medium was changed to serum-free medium Mo (MCDB 110 basal medium supplemented with insulin, transferrin, and sodium selenite; Sigma Diagnostics, Sigma-Aldrich)[23] for 24 hours and the cells treated with 2 μg/mL LPS (Sigma #L4391; Sigma-Aldrich) or 50 μg/mL poly I:C (Sigma #P0913; Sigma-Aldrich) in Mo medium for either 6 hours for RNA analysis or 24 hours. For harvesting conditioned medium for protein and zymography analysis, media from untreated and treated heterozygous and null cells were collected and either trichloroacetic acid precipitated for Western blot analysis or concentrated in an Amicon Ultra-4 centrifugal filter (EMD Millipore, Billerica, MA).

Superarray Analysis

RNA from either poly I:C− or LPS-treated *Wfdc1*-heterozygous and null mouse stromal cells was isolated (RNeasy Mini Kit; Qiagen, Valencia, CA). An oligo GEArray DNA microarray to Mouse Autoimmune and Inflammatory response (#OMM-803) and to the Toll-like receptor pathway (#OMM-018.2) were used (SABiosciences, Frederick, MD). Gene-specific primers for *Spp1* were purchased from Qiagen (#QT00157724). For superarray analysis of *Wfdc1* KO/KI stromal heterozygous and null stromal cell spheroids, the Mouse Extracellular Matrix and Adhesion Molecules (#OMM-013; SABiosciences) microarray was used. Hybridization and digital analysis were performed according to the manufacturer's protocol.

RT-PCR and Quantitative PCR Analysis

For reverse transcription of mRNA, 500 ng of stromal cell RNA was reverse-transcribed using the Superscript III kit (Invitrogen) in 20 μL of reaction. For quantitative PCR analysis, the RT reaction was diluted 1:5, and 5 μL was used in a 96-well plate with the FastStart Universal SYBR Green Master (Rox) kit (#04913914001; Roche, Basel, Switzerland) in 25 μL of final volume. An ABI 7700 instrument (Life Technologies) was used with the following program: 95°C for 10 minutes and then 40 cycles of 95°C for 15 seconds and 60°C for 30 seconds. mRNA expression was quantitated relative to *Gapdh* mRNA levels, and analysis of the real-time PCR was performed using the ΔΔCT method.[24]

Zymography and Western Blotting

Three *Wfdc1*-heterozygous stromal cell lines (HetMP1, HetMP3, and HetMP5) and two *Wfdc1*-null stromal cell lines (312#1L1 and 312#2P1) were treated with LPS or poly I:C as described above for 24 hours. Conditioned medium was collected and concentrated in an Amicon Ultra-4 centrifugal filter for zymography assays or concentrated by 10% trichloroacetic acid precipitation for Western blotting. For zymography, one-third of the concentrated medium was run on Bio-Rad ready-cast 10% gelatin gels (Bio Rad Laboratories, Hercules, CA), and stained with Coomassie Blue R-250 (Bio Rad Laboratories). For Western blotting, one-third of the trichloroacetic acid−precipitated conditioned medium was resuspended in 1× Nupage LDS sample buffer (Invitrogen) and run on a 10% Nupage Bis-Tris precast gel (Invitrogen) under reducing conditions. Following transfer to a PVDF membrane using the iBlot transfer apparatus (Invitrogen), the membrane was blocked in Roche Western blocking reagent for 1 hour, incubated in anti-mouse osteopontin (R&D Systems #AF808) at 0.2 μg/mL at 4°C O/N, followed by incubation in biotin-conjugated donkey anti-goat antibody (Invitrogen #D20698) at 1:1000 dilution for 1 hour at room temperature, and then incubated in Streptavidin-HRP (#RPN1239V; GE Healthcare, Chalfont St Giles, UK) at 1:5000 dilution for 45 minutes at room temperature. The blot was visualized using the Pierce ECL substrate and scanned with a Kodak Image Station 4000R

(Kodak, Rochester, NY) with Carestream version 5 software (Carestream Health, Rochester, NY).

In Vivo Wounding Assay and Immunostaining of Skin Wounds

Two 3-mm-diameter punch biopsy lesions were made on the flanks of *Wfdc1*-heterozygous and null mice. A total of at least five animals with two biopsies each were used to evaluate the wound healing over 7 days in each group. From day 1 to 7, the wounds were measured with calipers. The subsequent measurements were analyzed using a two-way analysis of variance analysis in GraphPad Prism version 5.0a. An additional five to seven mice per genotype were wounded, and at day 7, wounds were excised, fixed in 4% paraformaldehyde O/N, and prepared for paraffin sections as described above. Sections were stained with Masson's trichrome (Sigma #HT-15) and 4× images acquired. Measurements of the wound border were made using the Nuance software platform v.3.0.0 (PerkinElmer, Hopkinton, MA). Wound gap measurements were analyzed using a *t*-test analysis in GraphPad Prism. Sections of the 7-day wounds were stained for anti-F4/80 (BioLegend #122601) at 1:50 dilution O/N at 4°C with citrate retrieval, images deconvoluted (Nuance system) to separate the red stain (F4/80) from the blue hematoxylin stain, and the intensity overlap between the red and blue calculated.

The calculated overlap intensity was then analyzed by a *U*-test in GraphPad Prism. Additionally, 7-day wounds were stained with anti−Ki-67 antibody (SP6 NeoMarkers RM-9106-S0; NeoMarkers, Fremont, CA) at 1:200 dilution O/N at 4°C with citrate retrieval. Images were deconvoluted to separate the red stain (Ki-67) from the blue hematoxylin stain, and the intensity overlap between the red and blue calculated. The calculated overlap intensity was then analyzed by a *U*-test in GraphPad Prism. Finally, the 7-day skin wounds were stained with anti-osteopontin (Abcam #ab8448) at 1:200 dilution O/N at 4°C and images acquired. All IHC staining of the skin wounds used NovaRED (Vector Laboratories) as the substrate for the peroxidase-conjugated enzyme, either HRP-conjugated anti-rabbit (Epitomics #3051-1; Abcam) for rabbit antibodies or Streptavidin-HRP (Vector Laboratories), and Mayer's hematoxylin as the counterstain.

In Vitro Scratch and Adhesion Assay

Wfdc1-heterozygous and null stromal cell lines were grown to confluence in 6-well plates. Three pipette tips were attached to a multichannel pipette, and three even scratches in the monolayer were made per well. Images of the scratch were taken at ×10 or ×20 at 0, 9, or 16 hours with a Spot RT camera (SPOT Imaging Solutions, Sterling Heights, MI) attached to a Nikon T300 inverted microscope (Nikon, Tokyo, Japan). Using the Spot software version 5.0, the scratch width was measured and analyzed using a *t*-test in GraphPad Prism. The measurements were averaged from two different *Wfdc1*-heterozygous and two different *Wfdc1*-null lines, and the assay was performed two independent times in triplicate with three scratches per well.

For the anti-osteopontin migration inhibition assay, two *Wfdc1*-null stromal cell lines 312#2P1 and 312#2L4 were used in a scratch assay with the addition of either 10 μg of IgG isotype control, or 10 or 20 μg of anti-osteopontin (R&D Systems #AF808) added at time 0 hours following the scratch. At 10 hours post scratch, images of the wound width were photographed and analyzed as above. The anti-osteopontin migration inhibition assay was performed in triplicate with three scratches per well two independent times. The scratch width in each image was measured in at least three different places along the scratch. Individual *t*-tests were performed comparing the control IgG with either 10 or 20 μg of anti-osteopontin IgG with both cell lines.

For the adhesion assay, two *Wfdc1*-heterozygous cell lines (HetMA3 and Het MP1) and two *Wfdc1*-null cell lines (312#2P1 and 312#2P4) were plated at 1000 cells/well on 96-well strips from a Millicoat ECM Screening Kit (Millipore #ECM101-105) that contains individual 8-well strips coated with either fibronectin, laminin, vitronectin, collagen type I, or collagen type IV. The assay was performed according to the manufacturer's directions and read at OD 540 nm with a Bio-Rad iMark microplate reader. The adhesion assay was performed in duplicate and repeated three independent times. Two-way analysis of variance test with Bonferroni post-tests was performed to compare the OD 540-nm measurements of the extracellular matrix component for each *Wfdc1*-heterozygous cell line versus each *Wfdc1*-null line.

Results

Phenotype of *Wfdc1*-Null Mice and Spatial Expression of *Wfdc1*

To generate *Wfdc1*-null mice, exon 1 of the *Wfdc1* gene was deleted and the bacterial *lac*Z gene knocked in to the *Wfdc1* locus to trace expression using homologous recombination as described in Figure 1A. The resulting *Wfdc1*-heterozygous and homozygous null mice were evaluated for altered developmental or adult tissue phenotypes. *Wfdc1*-heterozygous and null mice exhibited no overt gross morphological or abnormal tissue phenotypes during either embryonic development or postnatal maturation. Reproductive rate, litter size, and sex ratios of *Wfdc1*-null mice were each normal. This normal-appearing phenotype is similar to null mice generated for other WAP family members.[25–27]

Owing to reports of mutant WFDC1/ps20 being associated with blindness, eye function was carefully evaluated. A complete electroretinogram analysis showed no overt physiological differences in retina function in *Wfdc1*-null and heterozygous mice (Supplemental Figure S1 and Supplemental Table S1). The spatial and temporal patterns of *Wfdc1* expression were evaluated by tracking the knockin nuclear β-gal reporter, constructed with a SV40 nuclear localization signal. Positive nuclear β-gal was observed in the adult mouse

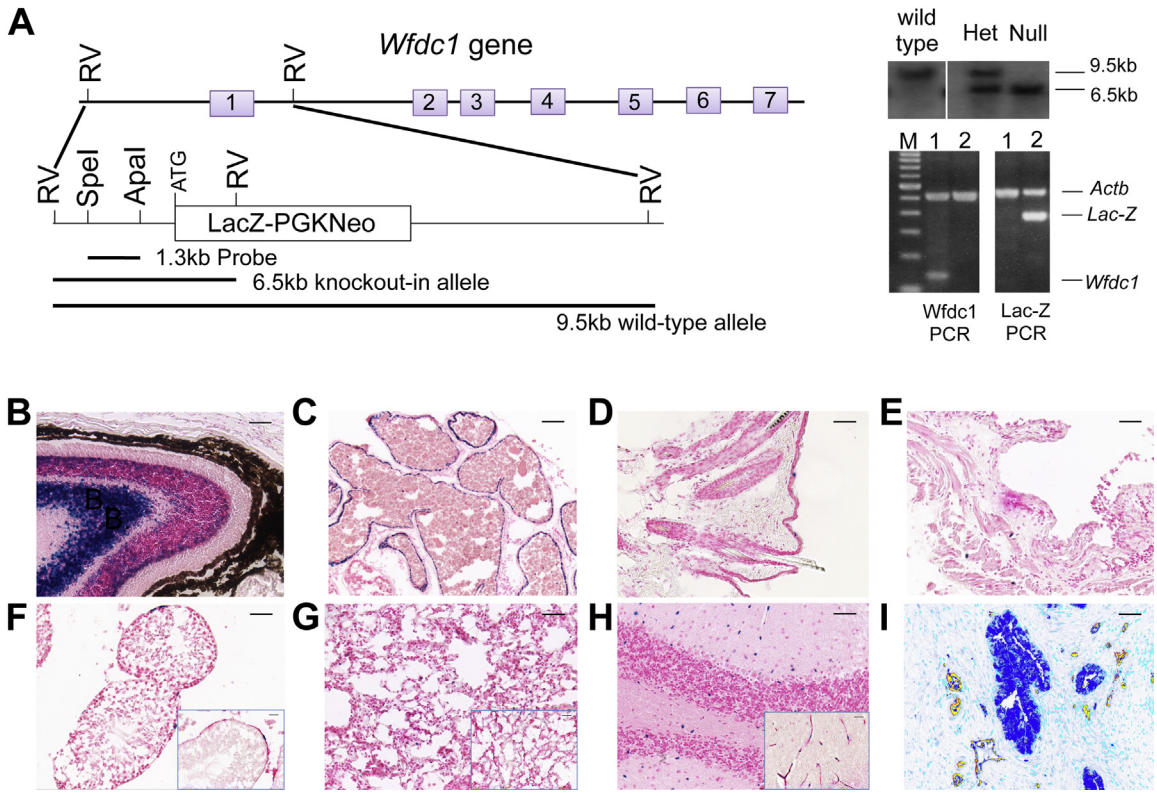

Figure 1 Generation of *Wfdc1* gene deletion and *LacZ* gene insertion at the ATG of the *Wfdc1* gene. **A:** The insertion of the LacZ-PGKNeo cassette adds an EcoRV site that is used to screen the mice by Southern analysis. Using a 1.3-kb probe, after digesting the genomic DNA with EcoRV, the knockout and wild-type alleles are 6.5 and 9.5 kb, respectively. Wild-type, heterozygous (Het), and Null lanes show 9.5-kb, 6.5- and 9.5-kb, and 6.5-kb bands, respectively. For subsequent PCR screening, *Actb*, *lacZ*, and *Wfdc1* primers produced a 500-bp, 364-bp, and 133-bp band, respectively. Lane 1 (wild-type) contains the Wfdc1 band, but no *lacZ* band. Lane 2 (*Wfdc1*-null mouse) shows *lacZ* band, but no *Wfdc1* band. *Wfdc1*-heterozygous mouse exhibits both a *Wfdc1* and *lacZ* band. **B**–**I:** Staining for Wfdc1 expression in mice and human prostate. Positive staining (blue precipitate) for reporter β-gal expression in frozen sections are observed in the inner nuclear layer and ganglion cell layers in the retina (**B**), the epithelial cells of the ventral prostate (**C**), sporadic cells in the epidermal layer of the skin (**D**), sporadic smooth muscle cells of the bladder (**E**), the endothelial cells of the testes (**inset** image is colocalization of β-gal staining in blue with CD34 in red) (**F**), endothelial cells of the lung alveoli (**inset** image is colocalization of β-gal staining in blue with anti-CD34 in red) (**G**), endothelial cells of the capillaries of the brain (**inset** image is colocalization of β-gal staining with anti-CD34 in red) (**H**), the epithelial cells in prostate acini and endothelial cells of vessels in the human prostate (colocalization of anti-ps20 in blue and anti-CD31 in red) (**I**). Scale bars: 50 μm (**main images**, **B**–**I**); 25 μm (**insets**, **F**–**H**).

retina (Figure 1B), prostate (Figure 1C), skin (Figure 1D), bladder (Figure 1E), testis (Figure 1F), lung (Figure 1G), and brain (Figure 1H), and in the human prostate gland (Figure 1I). Other mouse tissues such as the liver, spleen, thymus, kidney, and bone did not exhibit obvious nuclear β-gal staining. Of interest, β-gal staining was observed in cells within the walls of the microvasculature in many tissues.

Colocalization of β-gal expression with anti-CD34 demonstrated that *Wfdc1* expression was spatially associated with endothelial cells in small vessels in the brain, lung, and testes (Figure 1, F–H). *Wfdc1* expression was not spatially associated with either macrophages or type II pneumocytes in the lung (Supplemental Figure S2). In the retina, most cells in the inner nuclear layer and a few cells in the outer nuclear layer exhibited intense nuclear β-gal (Figure 1B). Epidermal cells of the skin and smooth muscle cells of the bladder exhibited sporadic expression of nuclear β-gal (Figure 1, D and E). Prostate gland exhibited a more general nuclear localization of β-gal in the acinar epithelial cells (Figure 1C). This spatial pattern of β-gal activity is consistent with immunolocalization of actual WFDC1/ps20 in the human prostate gland, where ps20 is spatially localized in prostate acinar epithelial cells and vascular, CD31-positive endothelial cells (Figure 1I). Together, these data are consistent with the notion that WFDC1/ps20 is localized to cells with a relatively high adhesive and barrier function. This includes endothelial cells where there is a blood–tissue barrier (brain and testis); lung, where the endothelial barrier is critically important; retina layers that exhibit high adhesion; and epithelial cells associated with barrier function in the prostate gland.

WFDC1 Affects Influenza Virus Infection

Owing to our previous studies that showed WFDC1/ps20 exhibits an immunomodulatory role that promotes HIV infection *in vitro*,[13] we investigated whether WFDC1/ps20 status affects influenza A infection in lung tissue. Wild-type, *Wfdc1*-heterozygous, and *Wfdc1*-homozygous null mice were subjected to lung infection with influenza A/TX. Remarkably, viral titers in lung tissue at 4 days postinfection showed a 2.75–log-fold lower titer in *Wfdc1*-null mice as compared to *Wfdc1*-heterozygous mice (Figure 2A)

($P < 0.005$). Viral titers in the wild-type mice were similar to *Wfdc1*-heterozygous mice. To assess whether levels of viral infectivity were associated with differences in immune cell infiltration, the 7-day postinfection lungs were evaluated for macrophage and neutrophil recruitment. A considerable elevation in macrophage recruitment was observed in the infected lung tissue in *Wfdc1*-null mice as compared to the infected wild-type and heterozygous lung tissue (Figure 2, B–D). No differences were observed in neutrophil immunoreactivity.

WFDC1 Affects Rate of Wound Closure

In addition to reports implicating the WAP-family members, Slpi[28] and elafin[29] in wound repair, we[8] have published that WFDC1/ps20 is down-regulated during reactive stroma formation in the progression of prostate cancer, where reactive stroma exhibits hallmarks of a wound repair response.[30–32] Accordingly, the *Wfdc1*-null and heterozygous mice were evaluated for alteration in wound repair subsequent to 3-mm–diameter full-thickness skin wounds. Evaluating wound gaps over a 7-day skin wound healing assay, *Wfdc1*-null mice exhibited a significant increase in rate of wound closure from days 5 to 7. By day 6, the wound gap in *Wfdc1*-null mice had significantly decreased to 46% of the starting wound gap as compared with a decrease to 62% of the starting gap in *Wfdc1*-heterozygous mice ($P < 0.05$) (Figure 3A). By day 7, *Wfdc1*-null mice exhibited 28% wound gap as compared with 46% in *Wfdc1*-heterozygous mice ($P < 0.05$). All tissues were harvested at day 7 and processed for IHC. Evaluation of wound repair tissues stained with Masson's trichrome, to assess reactive stroma, exhibited significant differences (Figure 3B). Measurements from microscopic evaluation of transverse sections showed that *Wfdc1*-null mice averaged a 1086-μm wound gap as compared with a 1400-μm wound gap for *Wfdc1*-heterogeneous mice ($P < 0.05$) (Figure 3B). IHC followed by deconvolution microscopy and quantitative image analysis showed a significant elevation and considerably more heterogeneity in macrophage recruitment in the *Wfdc1*-null mice (587 median OD value) as compared with the *Wfdc1*-heterozygous mice (200 median OD value) ($P < 0.05$) (Figure 3C). Similar to the lung infection experiments, no significant differences were observed in neutrophil infiltration. To determine the stage of wound repair, day 7 wounds were evaluated for Ki-67 staining by deconvolution microscopy and quantitative image analysis. During classical wound healing, cellular proliferation occurs during the second, or tissue formation, stage, whereas a decrease in proliferative cells occurs during the third, or tissue regeneration, stage.[33] A significant decrease in Ki-67 staining intensity was observed with the *Wfdc1*-null mice (13,772 median OD value) as compared with *Wfdc1*-heterozygous mice (24,537 median OD value) (Figure 3D). The lower Ki-67 staining intensity in both the epithelium and transitional stroma at day 7 in the *Wfdc1*-null mouse is consistent with a more advanced wound closure as compared with heterozygous mice.

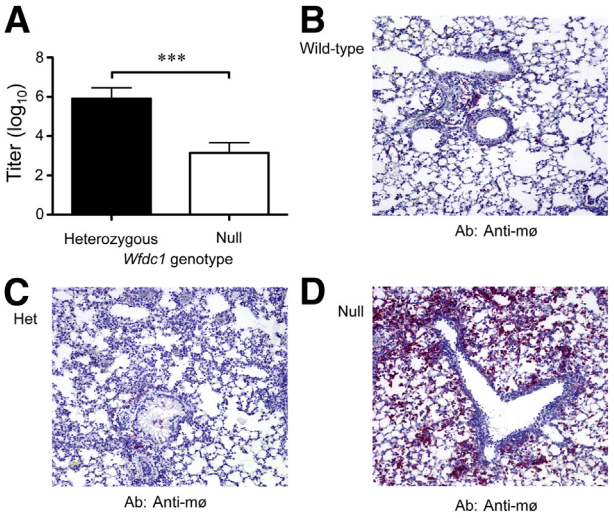

Figure 2 *Wfdc1*-null mice exhibit resistance to influenza virus infection concordant with an increase in macrophage recruitment. **A:** The *Wfdc1*-null mice exhibit a significant resistance to lung influenza A viral infection by 2.75-logs lower viral titer in lung tissue at day 4 postinfection. **B–D:** Immunohistochemistry for macrophage recruitment (anti-mø) shows elevated accumulation in day 7 *Wfdc1*-null mice infected lungs relative to day 7 control wild-type or *Wfdc1*-heterozygous (Het) mice infected lungs. Error bars show the standard error of the mean. ***$P < 0.005$. Original magnification: ×200 (**B–D**). Ab, antibody.

Elevated *Spp1* Osteopontin Expression in *Wfdc1*-Null Cells

To assess mechanisms of WFDC1/ps20 action in mediating inflammatory responses, fibroblast cell lines were derived from *Wfdc1*-null and heterozygous mice. To evaluate differential inflammatory responses, the cell lines were treated with either LPS or poly I:C to simulate bacterial and viral infections, respectively. Gene expression profiling revealed an enhanced inflammatory gene expression signature (Supplemental Figure S3). Genes differentially up-regulated in *Wfdc1*-null cells included tumor necrosis factor-α (TNF-α), IL-1β, IL-12β, granulocytic macrophage colony stimulating factor 3 (GM/CSF3), and Cox 2 (prostaglandin E synthase, *Ptges*). Of interest, expression of keratinocyte chemokine (KC) (murine homolog of IL-8) in response to both poly I:C and LPS was not induced nearly as high in *Wfdc1*-null cell lines (approximately 40-fold less) as compared to *Wfdc1*-heterozygous cell lines (Supplemental Figure S4). The *FGFR1* gene did not show an increased expression in response to the inflammatory agents LPS and poly I:C.

We have reported previously that WFDC1/ps20 regulates differential cell piling and cell shape in prostate smooth muscle cell lines.[5] In addition, elevated WFDC1/ps20 expression was associated with cell adhesion in spheroid formation in cultures of prostate stromal cells.[3] Accordingly, we evaluated expression profiles of genes encoding cell adhesion proteins, both in the context of a proinflammatory stimulus and in the context of spheroid formation, to assess alterations associated with *Wfdc1*-null conditions. This

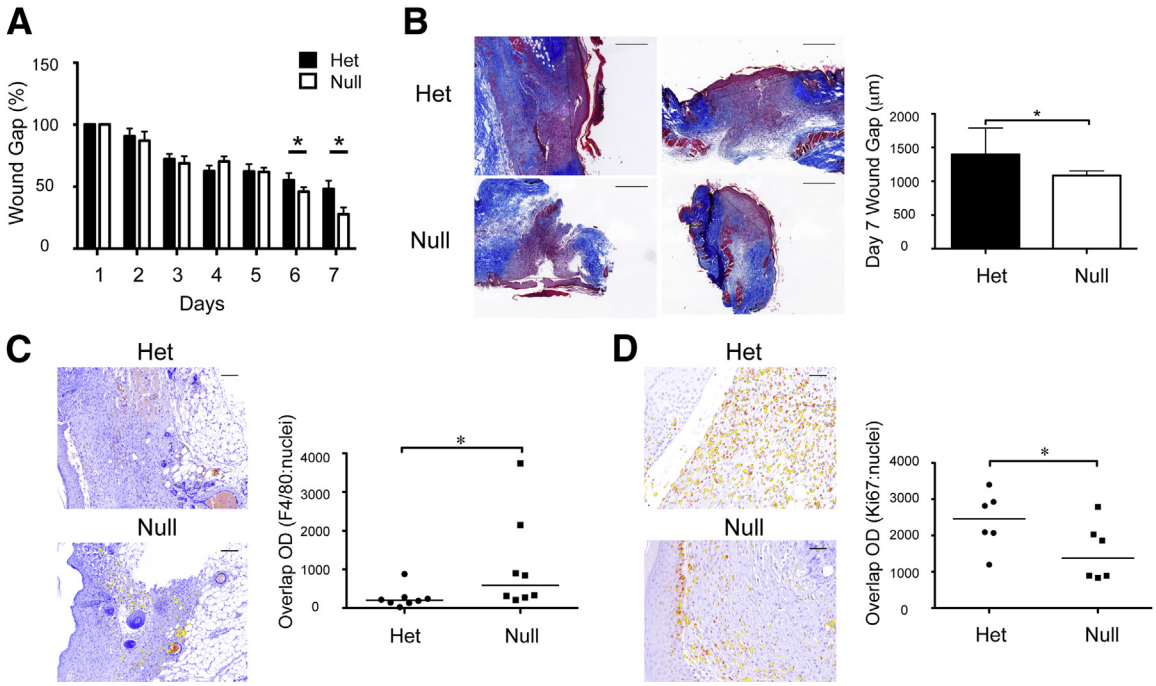

Figure 3 *Wfdc1*-null mice exhibit an elevated wound repair response concordant with an increase in macrophage recruitment. **A:** A significant difference in wound closure is observed in *Wfdc1*-null mice at days 6 and 7 relative to *Wfdc1*-heterozygous (Het) mice. **B:** Representative 4× trichrome images of the 7-day wounds of heterozygous and null mice were used to measure the wound gap (**measurement lines** are shown in the images). Quantitative analysis of the wound gap shows that wounds *of Wfdc1*-null mice exhibit a significantly elevated rate of closure as compared with heterozygous mice. **C:** Using the Nuance multispectral camera, micrographs (representative images) were analyzed using the Nuance software to calculate the percent F4/80-positive staining (red) that colocalized with nuclei (blue, hematoxylin; colocalization, yellow). Quantitative analysis of the overlap staining intensity (colocalization) shows that the 7-day skin wound of *Wfdc1*-null mice contains significantly more macrophage as compared with heterozygous mice. **D:** Micrographs (representative images) were analyzed quantitatively to calculate the percentage of Ki-67 (red) immunostaining that colocalized with nuclei (blue, hematoxylin; overlap, yellow). *Wfdc1*-null mice 7-day skin wounds contain significantly fewer Ki-67 staining cells as compared with heterozygous mouse 7-day skin wounds, reflecting a more completed repair process. Error bars show the standard error of the mean. $*P < 0.05$ (**A**—**D**). Scale bars: 500 μm (**B** and **C**).

revealed that in *Wfdc1*-null conditions, *Opn* (*Spp1*) was the only adhesion-related gene that was up-regulated in both inflammatory conditions (poly I:C treatment) and during spheroid formation (hanging-drop cultures) (Figure 4, A and B). *Opn* expression was up-regulated 62-fold higher in *Wfdc1*-null cells relative to *Wfdc1*-heterozygous cells after exposure to poly I:C (Figure 4A). Western blot analysis showed that *Wfdc1*-heterozygous cells secreted very little osteopontin, whereas *Wfdc1*-null fibroblasts secreted both more full-length and cleaved osteopontin protein, known to be the activated forms (Figure 4B). Osteopontin levels also correlated with the ability to form spheroids in hanging-drop cultures. *Wfdc1*-heterozygous cells formed typical spheroids in hanging-drop cultures (Figure 4C). However, *Wfdc1*-null cells were completely restricted from spheroid formation in hanging-drop cultures, were negative for nuclear reporter β-gal during spheroid culture conditions, and exhibited a 2.3-fold elevation in *Opn* message relative to *Wfdc1*-heterozygous cell spheroids (Figure 4C).

Owing to the elevated expression in *Wfdc1*-null cells, IHC for osteopontin was evaluated in the influenza A—infected lungs and in day 7 wound repair tissues to determine whether elevated osteopontin protein associated with the null phenotype. Consistent with the *in vitro* findings, considerably more intense osteopontin immunoreactivity was observed in both the influenza-infected lung tissue and the 7-day skin wound tissue in the *Wfdc1*-null mice relative to *Wfdc1*-heterozygous mice (Figure 4D).

Wfdc1-Null Cell Lines Exhibit Rapid Migration/Closure and Altered Adhesion Properties *in Vitro*

Consistent with the *in vivo* data, *Wfdc1*-null cells *in vitro* exhibited significantly elevated migration in wounding scratch assays in culture, as compared with *Wfdc1*-heterozygous cells (Figure 5A). At 9 hours, *Wfdc1*-null cells exhibited a significant increase in closure and had migrated an average of 506 μm as compared with an average of 244 μm with the heterozygous cell lines ($P < 0.005$). *Wfdc1*-null cells achieved near full closure by 16 hours (655-μm migration), whereas the *Wfdc1*-heterozygous lines displayed significantly less closure (516 μm) ($P < 0.005$) (Figure 5A). To assess whether the increased migration of *Wfdc1*-null cells was attributable to elevated osteopontin activity, neutralizing antibody was added to two different null cell lines (P1 and L4) subsequent to scratch wounding. Osteopontin neutralizing antibody inhibited wound closure in the P1 *Wfdc1*-null line relative to control at both 10 μg (358-μm migration)

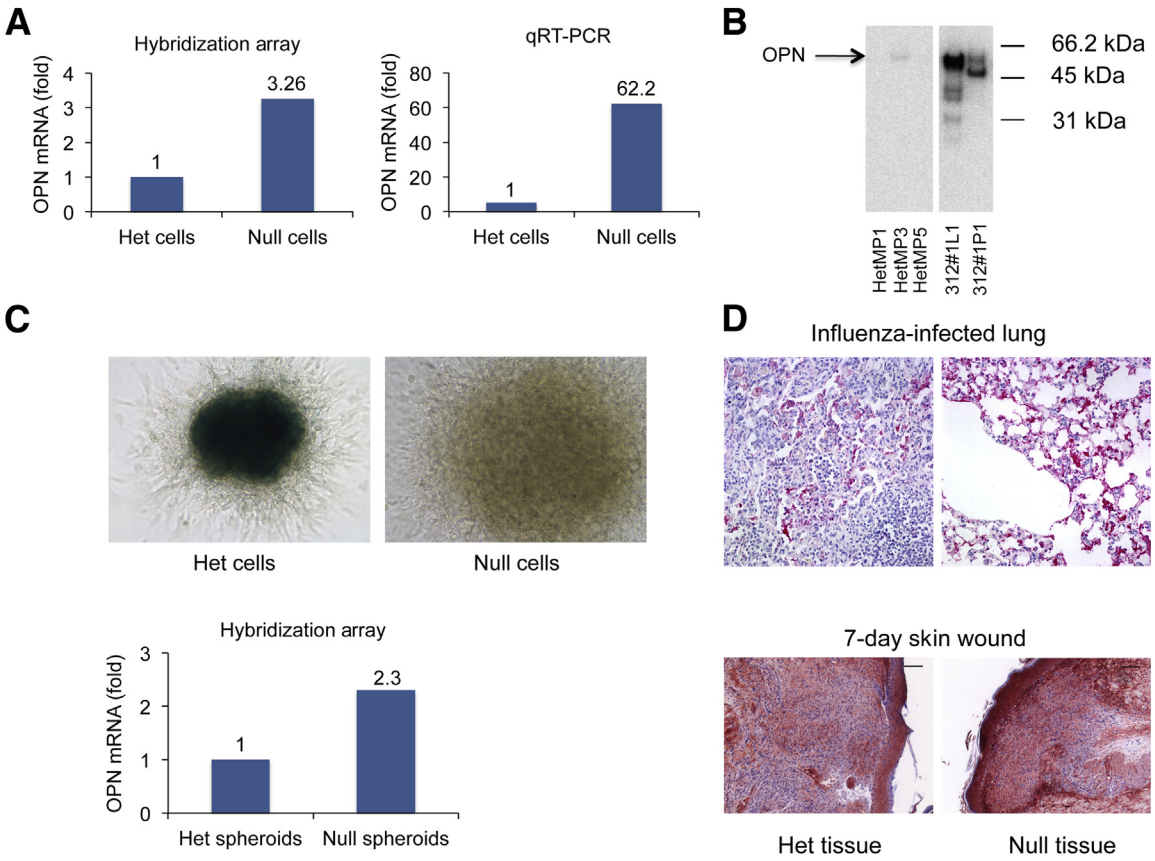

Figure 4 Elevated message and protein expression of osteopontin in *Wfdc1*-null stromal cell lines, influenza-infected *Wfdc1*-null lungs, and *Wfdc1*-null 7-day skin wounds. **A:** Expression of osteopontin mRNA is elevated 3.26-fold in poly I:C—treated *Wfdc1*-null cells as compared with poly I:C—treated *Wfdc1*-heterozygous (Het) cells as assessed by hybridization arrays. Quantitative PCR (qRT-PCR) analysis of poly I:C—treated *Wfdc1*-null stromal cells verifies that osteopontin mRNA is increased 62.2-fold relative to poly I:C—treated *Wfdc1*-heterozygous stromal cells. **B:** Three *Wfdc1*-heterozygous stromal cell lines (HetMP1, -3, and -5) show relatively low levels of osteopontin protein (OPN) secreted into conditioned media. Comparatively, the *Wfdc1*-null stromal cell lines (312#1L1 and 312#1P1) show an increase in full-length osteopontin (**arrow**) and cleavage products. **C:** Spheroids were formed in hanging-drop cultures for 4 to 5 days, plated, and then stained for β-gal expression (blue). *Wfdc1*-null cells were restricted from spheroid formation and did not stain for reporter β-gal expression as compared with tight spheroidal organization and positive β-gal staining in hanging-drop cultures generated with *Wfdc1*-heterozygous stromal cells. Screening an extracellular matrix and adhesion molecule expression array from SABiosciences shows a 2.3-fold increase in osteopontin expression in the null spheroids. **D:** IHC reveals an elevated staining intensity for osteopontin (red) in *Wfdc1*-null infected lungs and 7-day skin wounds as compared with *Wfdc1*-heterozygous tissue controls. Original magnification, ×200 (**C** and **D**).

and 20 μg (303-μm migration) concentrations relative to control conditions (458-μm migration) (Figure 5B) ($P < 0.01$). In the L4 cell line, osteopontin neutralizing antibody again significantly inhibited at 10 μg (257-μm migration) and 20 μg (179-μm migration) relative to control conditions (395-μm migration) (Figure 5B). No significant differences were found in cell proliferation of the *Wfdc1*-null cells as compared with the *Wfdc1*-heterozygous cells *in vitro*. Together, these results suggest that *Wfdc1*-null cells exhibit elevated cell migration and that this was mediated by elevated osteopontin secreted by the *Wfdc1*-null cells.

Because wound repair migration is affected by differential cell adhesion and contraction, adhesion to several matrix proteins that are expressed at sites of wound repair was evaluated. Of these, the *Wfdc1*-null cell lines exhibited significantly increased adhesion to both fibronectin and laminin relative to *Wfdc1*-heterozygous cells (Figure 5C). However, no changes were observed in cell adhesion to vitronectin, collagen I, or collagen IV.

Wfdc1-Null Cells Express Elevated MMP-9 Activity

Several studies have implicated MMP activity in osteopontin-mediated adhesion and migration.[34–36] Moreover, MMP-9 has been shown to cleave osteopontin into fragments that promote cell migration and the metastatic potential of cancer cells.[37,38] Hence, we evaluated whether MMP activity was altered in *Wfdc1*-null cells. Elevated levels of biologically active forms of MMP-9 were found in *Wfdc1*-null cell lines (312#1L1 and 312#1P1) as compared with *Wfdc1*-heterozygous cell lines (HetMP1, -3, and -5) as shown by gelatin zymography (Figure 6A). By contrast, the levels of MMP-2 were similar in all cell lines, irrespective of *Wfdc1* status. Interestingly, the levels of active MMP-9 in *Wfdc1*-null cells in steady-state conditions were similar to

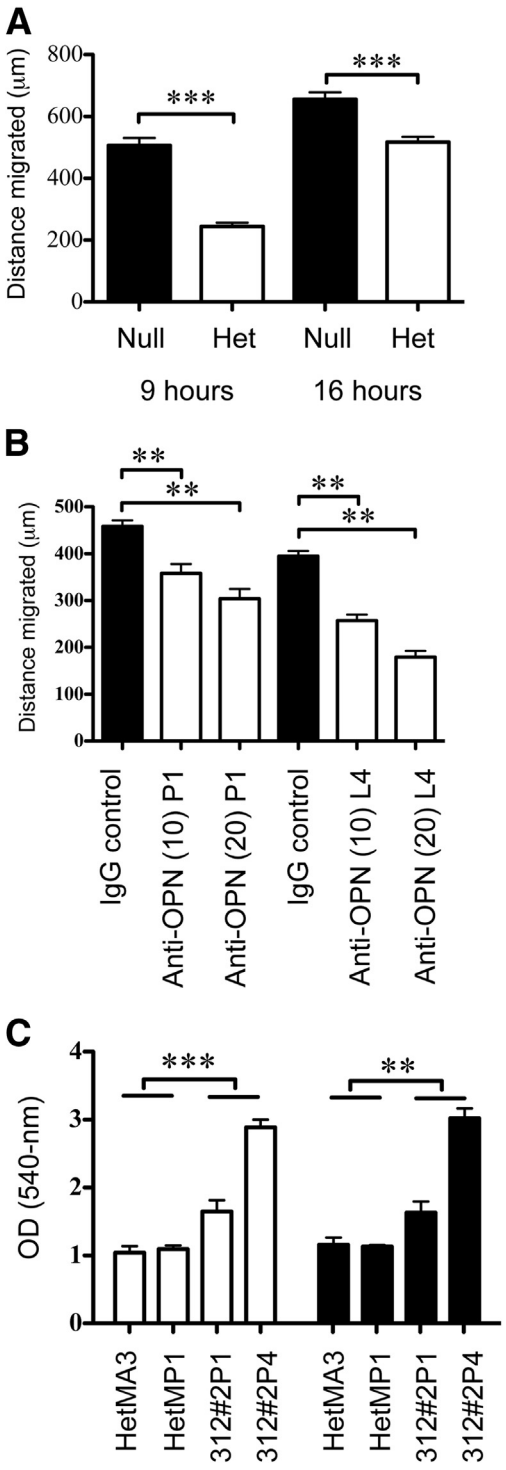

Figure 5 Elevated cell migration and adhesion properties in *Wfdc1*-null stromal cells. **A:** *Wfdc1*-null stromal cells exhibit significant increase in closure rates of *in vitro* scratch assays at both 9 and 16 hours relative to *Wfdc1*-heterozygous cells ($P < 0.005$). **B:** Incubation with osteopontin (OPN) neutralizing antibody (at both 10 and 20 μg) significantly decreases *in vitro* wound closure in two independent null cell lines (312#P1 and 312#2L4) relative to an IgG control antibody ($P < 0.01$). **C:** *Wfdc1*-null stromal cell lines (312#2P1 and 312#2P4) display significantly more adhesion to both fibronectin and laminin compared to *Wfdc1*-heterozygous stromal cell lines (HetMA3 and HetMP1). Error bars show the standard error of the mean. Black bars, laminin; white bars, fibronectin. $^{**}P < 0.01$, $^{***}P < 0.005$.

levels in LPS-treated conditions, showing that *Wfdc1*-null cells not only exhibit a higher level of osteopontin, but also express constitutively active MMP-9 as compared with *Wfdc1*-heterozygous cell lines. Although activation levels were different, there appeared to be similar levels of total protein irrespective of *Wfdc1* status. IHC analysis of MMP-9 in infected lung tissue showed that immunoreactivity was approximately the same in the wild-type, *Wfdc1*-heterozygous, and *Wfdc1*-null influenza-infected lung tissue (Figure 6B), suggesting the level of total protein expression does not differ in the infected lung tissue. These data suggest that MMP-9 protein is constitutively active in *Wfdc1*-null conditions even though total protein is similar to *Wfdc1*-heterozygous conditions. These data may explain the elevated levels of cleaved (activated) osteopontin observed in *Wfdc1*-null conditions, because MMP-9 is known to cleave and produce osteopontin fragments that promote cell migration/invasion.[38]

Discussion

Interestingly, knockout of *Wfdc1* resulted in no overt developmental or adult tissue phenotype, similar to what has been reported for other WAP family members. However, differential biological responses were evident during challenges to homeostasis in adult tissues. Importantly, *Wfdc1*-null mice exhibited a significant elevation in resistance to influenza A virus infection and a more rapid cutaneous wound repair response. Both these responses were associated with elevated recruitment of macrophages and elevated expression of osteopontin. Moreover, *Wfdc1*-null cells exhibited elevated secretion of constitutively active MMP-9, an enzyme that is important in osteopontin processing to active fragments among other biological activities.[37] Consistent with this notion, elevated expression of both full-length and cleaved osteopontin was observed in the *Wfdc1*-null condition. The cleaved osteopontin fragments have been associated with elevated migration and metastasis in cancer. *Wfdc1*-null cells *in vitro* also exhibited altered adhesion and rapid closure in scratch assays, consistent with *in vivo* results. Together, these results suggest that *Wfdc1* is not likely involved in embryological development or adult normal steady-state biology; however, it is a key repressor and modulator of critical aspects of response mechanisms that operate during disrupted tissue homeostasis. As such, *Wfdc1* may be one of the genes best described as being associated with modulating emergency biology. Consistent with this suggestion, osteopontin has also been shown to be associated with a wide variety of emergency biology responses.

Osteopontin is a matricellular protein expressed by a number of cell types, including macrophages, smooth muscle, endothelial cells, and retinal Müller cells.[39,40] In addition, osteopontin is important in wound repair, fibrosis resolution, and host responses to microbial infection.[41–43] Osteopontin is

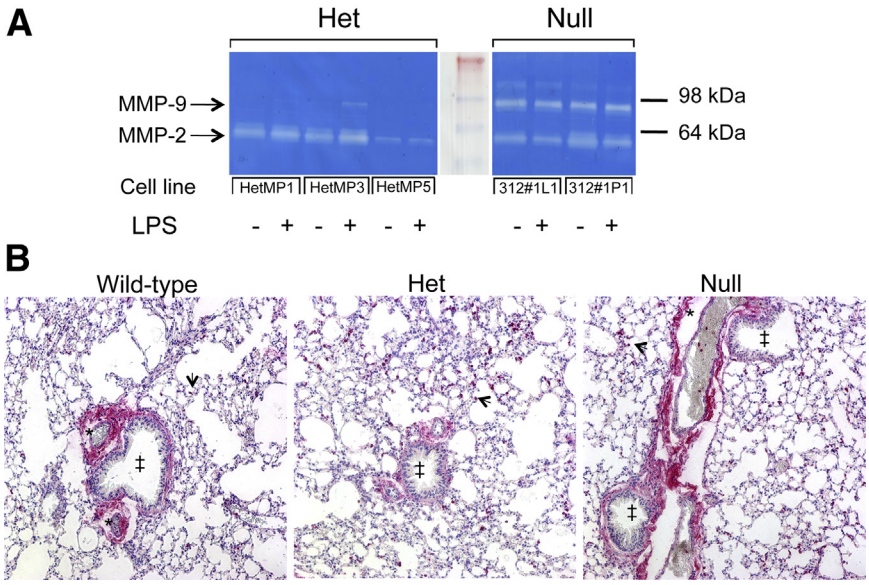

Figure 6 Increased gelatinase activity in untreated *Wfdc1*-null cells. **A:** Three *Wfdc1*-heterozygous (Het) stromal cells lines express MMP-2 at nearly similar levels when untreated or treated with lipopolysaccharide (LPS), whereas *Wfdc1*-null stromal cell lines also express increased MMP-9 activity in both untreated and LPS-treated conditions. **B:** IHC for MMP-9 (red) in *Wfdc1* wild-type, heterozygous, and null influenza–infected lungs shows similar staining intensity and localization of staining in vessels (**asterisks**), bronchioles (**double daggers**), and macrophages (**arrows**). Original magnification, ×200 (**B**).

a potent chemokine in the recruitment of macrophages during inflammatory reactions[41,44] and in modulating cell migration/invasion.[37,38] The biological responses noted in *Wfdc1*-homozygous null conditions are fully consistent with elevated osteopontin activity, including altered cell migration, adhesion, spheroid formation *in vitro*, and recruitment of macrophages. This was particularly evident in the day 6 and day 7 wound repair study, where the timeline of more rapid closure was congruent with elevated osteopontin and macrophage recruitment. Osteopontin has not been previously associated with WAP family members. Considerable heterogeneity was observed in the elevated macrophage recruitment in the *Wfdc1*-homozygous null conditions, and this may relate to elevated osteopontin expression. How osteopontin and macrophages may affect wound contraction by myofibroblasts is not yet understood. However, osteopontin has been shown to be required for TGF-β1–induced myofibroblast differentiation.[45] Hence, the more rapid wound repair in *Wfdc1*-null mice could result, in part, from the actions of elevated osteopontin on myofibroblast differentiation or function. It follows that low expression of WFDC1/ps20 observed at sites of reactive stroma[8] may be associated with myofibroblast biology, known to be important in reactive stroma.

The observation that basal MMP-9 activity was increased in *Wfdc1*-null cells is consistent with the biology observed in the *Wfdc1*-null mice. Osteopontin has been shown to up-regulate MMP-9 expression,[35] and macrophage- and epithelial cell-derived MMP-9 cleaves osteopontin.[46] Other WAP family members, SLPI and WFDC2, can also modulate the activity of MMP-9.[47–49] Moreover, inflammatory macrophage migration is dependent on plasminogen-cleaved MMP-9.[50] Observing both up-regulated MMP-9 activity and osteopontin overexpression and cleavage in the LPS-treated *Wfdc1*-null cells establishes *Wfdc1* as a modulator of this osteopontin–MMP-9 axis. Furthermore, we have shown that WFDC1/ps20 expression in the stromal compartment in human prostate cancer is decreased, whereas cancer/epithelial expression is increased; however, cancer cells were shown to express a novel splice variant of *WFDC1*.[8,51] Hence, it is possible that altered WFDC1/ps20 expression modulates cancer cell migration/invasion, which could affect metastasis.

As determined by the knockin reporter, expression of *Wfdc1* was observed in cells that exhibit a high adhesive, barrier function, among other features: notably, endothelial cells at the blood–brain barrier, endothelial cells at the blood–testis barrier, skin epidermal cells, prostate epithelium, retina layers, and smooth muscle in the bladder. Corroborating the brain endothelial–specific expression, another study identified *Wfdc1* as both a blood–brain barrier and endothelial-enriched transcript relative to peripheral endothelial cells and pericytes.[52] The expression in the retinal inner nuclear layer is consistent with an additional study that showed that *Wfdc1* is in the top 11% of genes that are expressed in the inner nuclear layer–specific Müller cells.[53] In addition, localization of WFDC1/ps20 changed during retinal development in *Chx10*-null mice, where *Chx10* has been shown to be a retinal progenitor cell and Müller cell–specific gene.[53,54] Together, these data suggest that WFDC1/ps20 is likely an important regulator of retina biology, although we did not observe vision-related phenotypes associated with *Wfdc1*-null conditions.

WFDC1 is unique among the human WAP family members. *WFDC1* is not located in chromosome 20q13, which contains 19 genes with either a WAP or Kunitz-type domain in a region shown to undergo strong genetic selective pressure.[55–57] Most of the 20q13 WAP genes, such as *SLPI* and *PI3* (SKALP, elafin), exhibit antimicrobial activity and antiprotease activity.[6,7] Most of the 20q13 WAP genes are up-regulated following changes in tissue

homeostasis and appear to attenuate the innate host response.[58–60] By contrast, WFDC1/ps20 is down-regulated in cancer, specifically in the stroma,[8,51,61–64] and stimulates response mechanisms. WFDC1/ps20 was down-regulated in two models of *in vivo* activation of hepatic stellate cells, which are cells most responsible for liver fibrosis.[65] We have now shown that *Wfdc1*-null mice exhibited augmented tissue repair/inflammatory responses during both influenza infection and skin wound repair. It could be surmised that down-regulated expression or activity of WFDC1/ps20 is required in barrier cells to signal-activated tissue responses leading to recruitment of infiltrating cells. In addition to expressing more proinflammatory chemokines, like osteopontin, these cells also express other WAP family members such as *SLPI* and *PI3*. *Wfdc1*-null cells also expressed an increased inflammatory gene profile, however with a conspicuous lack of KC overexpression. The other WAP family members that have been studied seem to regulate IκB degradation and subsequent NF-κB signaling.[66] The lack of a full proinflammatory gene profile argues against WFDC1/ps20 regulating the NF-κB signaling pathway in the same way as the other WAP family members, although this requires further study.

The present report suggests that WFDC1/ps20 is a fundamental regulator of diverse inflammatory and wound repair responses. Elevated or basal levels of WFDC1/ps20 would be expected to sustain adult differentiated biology, whereas down-regulated WFDC1/ps20 expression or activity would induce a permissive switch to a repair/inflammatory biology that is required to clear microorganisms, and to affect a repair response typified by elevated stromal cell migration and matrix remodeling. Homeostasis after the repair might then be associated with a resumed expression or activity of WFDC1/ps20 and a return to an inflammatory-quiescent, adult differentiated biology state. Hence, determining the mechanisms that regulate *Wfdc1* expression and functions will help further elucidate how this protein and the downstream biology affects core responses and modulation of tissue homeostasis. These mechanisms will be important to the design of novel therapeutic approaches to treating microbial disorders, inflammatory responses, and altered wound repair responses.

Supplemental Data

Supplemental material for this article can be found at *http://dx.doi.org/10.1016/j.ajpath.2014.07.013*.

References

1. Rowley DR: Characterization of a fetal urogenital sinus mesenchymal cell line U4F: secretion of a negative growth regulatory activity. In Vitro Cell Dev Biol 1992, 28A:29–38
2. Rowley DR, Tindall DJ: Responses of NBT-II bladder carcinoma cells to conditioned medium from normal fetal urogenital sinus. Cancer Res 1987, 47:2955–2960
3. Rowley DR, Dang TD, Larsen M, Gerdes MJ, McBride L, Lu B: Purification of a novel protein (ps20) from urogenital sinus mesenchymal cells with growth inhibitory properties in vitro. J Biol Chem 1995, 270:22058–22065
4. Larsen M, Ressler SJ, Gerdes MJ, Lu B, Byron M, Lawrence JB, Rowley DR: The WFDC1 gene encoding ps20 localizes to 16q24, a region of LOH in multiple cancers. Mamm Genome 2000, 11: 767–773
5. Larsen M, Ressler SJ, Lu B, Gerdes MJ, McBride L, Dang TD, Rowley DR: Molecular cloning and expression of ps20 growth inhibitor. A novel WAP- type "four-disulfide core" domain protein expressed in smooth muscle. J Biol Chem 1998, 273: 4574–4584
6. Bouchard D, Morisset D, Bourbonnais Y, Tremblay GM: Proteins with whey-acidic-protein motifs and cancer. Lancet Oncol 2006, 7: 167–174
7. Bingle CD, Vyakarnam A: Novel innate immune functions of the whey acidic protein family. Trends Immunol 2008, 29:444–453
8. McAlhany SJ, Ayala GE, Frolov A, Ressler SJ, Wheeler TM, Watson JE, Collins C, Rowley DR: Decreased stromal expression and increased epithelial expression of WFDC1/ps20 in prostate cancer is associated with reduced recurrence-free survival. Prostate 2004, 61: 182–191
9. Barron DA, Rowley DR: The reactive stroma microenvironment and prostate cancer progression. Endocr Relat Cancer 2012, 19: R187–R204
10. Ressler SJ, Rowley DR: The WFDC1 gene: role in wound response and tissue homoeostasis. Biochem Soc Trans 2011, 39:1455–1459
11. Tuxhorn JA, Ayala GE, Rowley DR: Reactive stroma in prostate cancer progression. J Urol 2001, 166:2472–2483
12. McAlhany SJ, Ressler SJ, Larsen M, Tuxhorn JA, Yang F, Dang TD, Rowley DR: Promotion of angiogenesis by ps20 in the differential reactive stroma prostate cancer xenograft model. Cancer Res 2003, 63:5859–5865
13. Alvarez R, Reading J, King DF, Hayes M, Easterbrook P, Farzaneh F, Ressler S, Yang F, Rowley D, Vyakarnam A: WFDC1/ps20 is a novel innate immunomodulatory signature protein of human immunodeficiency virus (HIV)-permissive CD4+ CD45RO+ memory T cells that promotes infection by upregulating CD54 integrin expression and is elevated in HIV type 1 infection. J Virol 2008, 82: 471–486
14. Rogers E, Wang BX, Cui Z, Rowley DR, Ressler SJ, Vyakarnam A, Fish EN: WFDC1/ps20: a host factor that influences the neutrophil response to murine hepatitis virus (MHV) 1 infection. Antiviral Res 2012, 96:158–168
15. Abbasi AR, Khalaj M, Tsuji T, Tanahara M, Uchida K, Sugimoto Y, Kunieda T: A mutation of the WFDC1 gene is responsible for multiple ocular defects in cattle. Genomics 2009, 94:55–62
16. Radeke MJ, Peterson KE, Johnson LV, Anderson DH: Disease susceptibility of the human macula: differential gene transcription in the retinal pigmented epithelium/choroid. Exp Eye Res 2007, 85: 366–380
17. van Soest SS, de Wit GM, Essing AH, ten Brink JB, Kamphuis W, de Jong PT, Bergen AA: Comparison of human retinal pigment epithelium gene expression in macula and periphery highlights potential topographic differences in Bruch's membrane. Mol Vis 2007, 13:1608–1617
18. Committee for the Update of the Guide for the Care and Use of Laboratory Animals; National Research Council: Guide for the Care and Use of Laboratory Animals. Eighth Edition. Washington, DC, National Academies Press, 2011
19. Pennesi ME, Cho JH, Yang Z, Wu SH, Zhang J, Wu SM, Tsai MJ: BETA2/NeuroD1 null mice: a new model for transcription factor-dependent photoreceptor degeneration. J Neurosci 2003, 23:453–461

20. Barron DA, Strand DW, Ressler SJ, Dang TD, Hayward SW, Yang F, Ayala GE, Ittmann M, Rowley DR: TGF-beta1 induces an age-dependent inflammation of nerve ganglia and fibroplasia in the prostate gland stroma of a novel transgenic mouse. PLoS One 2010, 5:e13751
21. Schauer IG, Ressler SJ, Rowley DR: Keratinocyte-derived chemokine induces prostate epithelial hyperplasia and reactive stroma in a novel transgenic mouse model. Prostate 2009, 69:373−384
22. Tuxhorn JA, McAlhany SJ, Dang TD, Ayala GE, Rowley DR: Stromal cells promote angiogenesis and growth of human prostate tumors in a differential reactive stroma (DRS) xenograft model. Cancer Res 2002, 62:3298−3307
23. Gerdes MJ, Larsen M, Dang TD, Ressler SJ, Tuxhorn JA, Rowley DR: Regulation of rat prostate stromal cell myodifferentiation by androgen and TGF-beta1. Prostate 2004, 58:299−307
24. Livak KJ, Schmittgen TD: Analysis of relative gene expression data using real-time quantitative PCR and the 2(-Delta Delta C(T)) Method. Methods 2001, 25:402−408
25. Ashcroft GS, Lei K, Jin W, Longenecker G, Kulkarni AB, Greenwell-Wild T, Hale-Donze H, McGrady G, Song XY, Wahl SM: Secretory leukocyte protease inhibitor mediates non-redundant functions necessary for normal wound healing. Nat Med 2000, 6:1147−1153
26. Nakamura A, Mori Y, Hagiwara K, Suzuki T, Sakakibara T, Kikuchi T, Igarashi T, Ebina M, Abe T, Miyazaki J, Takai T, Nukiwa T: Increased susceptibility to LPS-induced endotoxin shock in secretory leukoprotease inhibitor (SLPI)-deficient mice. J Exp Med 2003, 197:669−674
27. Triplett AA, Sakamoto K, Matulka LA, Shen L, Smith GH, Wagner KU: Expression of the whey acidic protein (Wap) is necessary for adequate nourishment of the offspring but not functional differentiation of mammary epithelial cells. Genesis 2005, 43:1−11
28. Zhu J, Nathan C, Jin W, Sim D, Ashcroft GS, Wahl SM, Lacomis L, Erdjument-Bromage H, Tempst P, Wright CD, Ding A: Conversion of proepithelin to epithelins: roles of SLPI and elastase in host defense and wound repair. Cell 2002, 111:867−878
29. van Bergen BH, Andriessen MP, Spruijt KI, van de Kerkhof PC, Schalkwijk J: Expression of SKALP/elafin during wound healing in human skin. Arch Dermatol Res 1996, 288:458−462
30. Gabbiani G: The myofibroblast in wound healing and fibrocontractive diseases. J Pathol 2003, 200:500−503
31. Gabbiani G, Ryan GB, Majne G: Presence of modified fibroblasts in granulation tissue and their possible role in wound contraction. Experientia 1971, 27:549−550
32. Rowley DR: What might a stromal response mean to prostate cancer progression? Cancer Metastasis Rev 1998, 17:411−419
33. Gurtner GC, Werner S, Barrandon Y, Longaker MT: Wound repair and regeneration. Nature 2008, 453:314−321
34. Berman JS, Serlin D, Li X, Whitley G, Hayes J, Rishikof DC, Ricupero DA, Liaw L, Goetschkes M, O'Regan AW: Altered bleomycin-induced lung fibrosis in osteopontin-deficient mice. Am J Physiol Lung Cell Mol Physiol 2004, 286:L1311−L1318
35. Chen YJ, Wei YY, Chen HT, Fong YC, Hsu CJ, Tsai CH, Hsu HC, Liu SH, Tang CH: Osteopontin increases migration and MMP-9 up-regulation via alphavbeta3 integrin, FAK, ERK, and NF-kappaB-dependent pathway in human chondrosarcoma cells. J Cell Physiol 2009, 221:98−108
36. Rangaswami H, Kundu GC: Osteopontin stimulates melanoma growth and lung metastasis through NIK/MEKK1-dependent MMP-9 activation pathways. Oncol Rep 2007, 18:909−915
37. Takafuji V, Forgues M, Unsworth E, Goldsmith P, Wang XW: An osteopontin fragment is essential for tumor cell invasion in hepatocellular carcinoma. Oncogene 2007, 26:6361−6371
38. Anborgh PH, Mutrie JC, Tuck AB, Chambers AF: Pre- and post-translational regulation of osteopontin in cancer. J Cell Commun Signal 2011, 5:111−122
39. O'Brien ER, Garvin MR, Stewart DK, Hinohara T, Simpson JB, Schwartz SM, Giachelli CM: Osteopontin is synthesized by macrophage, smooth muscle, and endothelial cells in primary and restenotic human coronary atherosclerotic plaques. Arterioscler Thromb 1994, 14:1648−1656
40. Wahl V, Vogler S, Grosche A, Pannicke T, Ueffing M, Wiedemann P, Reichenbach A, Hauck SM, Bringmann A: Osteopontin inhibits osmotic swelling of retinal glial (Muller) cells by inducing release of VEGF. Neuroscience 2013, 246:59−72
41. Ashkar S, Weber GF, Panoutsakopoulou V, Sanchirico ME, Jansson M, Zawaideh S, Rittling SR, Denhardt DT, Glimcher MJ, Cantor H: Eta-1 (osteopontin): an early component of type-1 (cell-mediated) immunity. Science 2000, 287:860−864
42. Liaw L, Birk DE, Ballas CB, Whitsitt JS, Davidson JM, Hogan BL: Altered wound healing in mice lacking a functional osteopontin gene (spp1). J Clin Invest 1998, 101:1468−1478
43. Lorena D, Darby IA, Gadeau AP, Leen LL, Rittling S, Porto LC, Rosenbaum J, Desmouliere A: Osteopontin expression in normal and fibrotic liver. altered liver healing in osteopontin-deficient mice. J Hepatol 2006, 44:383−390
44. Giachelli CM, Lombardi D, Johnson RJ, Murry CE, Almeida M: Evidence for a role of osteopontin in macrophage infiltration in response to pathological stimuli in vivo. Am J Pathol 1998, 152:353−358
45. Lenga Y, Koh A, Perera AS, McCulloch CA, Sodek J, Zohar R: Osteopontin expression is required for myofibroblast differentiation. Circ Res 2008, 102:319−327
46. Tan TK, Zheng G, Hsu TT, Lee SR, Zhang J, Zhao Y, Tian X, Wang Y, Wang YM, Cao Q, Lee VW, Wang C, Zheng D, Alexander SI, Thompson E, Harris DC: Matrix metalloproteinase-9 of tubular and macrophage origin contributes to the pathogenesis of renal fibrosis via macrophage recruitment through osteopontin cleavage. Lab Invest 2013, 93:434−449
47. Choi BD, Jeong SJ, Wang G, Park JJ, Lim DS, Kim BH, Cho YI, Kim CS, Jeong MJ: Secretory leukocyte protease inhibitor is associated with MMP-2 and MMP-9 to promote migration and invasion in SNU638 gastric cancer cells. Int J Mol Med 2011, 28:527−534
48. Hoskins E, Rodriguez-Canales J, Hewitt SM, Elmasri W, Han J, Han S, Davidson B, Kohn EC: Paracrine SLPI secretion upregulates MMP-9 transcription and secretion in ovarian cancer cells. Gynecol Oncol 2011, 122:656−662
49. LeBleu VS, Teng Y, O'Connell JT, Charytan D, Muller GA, Muller CA, Sugimoto H, Kalluri R: Identification of human epididymis protein-4 as a fibroblast-derived mediator of fibrosis. Nat Med 2013, 19:227−231
50. Gong Y, Hart E, Shchurin A, Hoover-Plow J: Inflammatory macrophage migration requires MMP-9 activation by plasminogen in mice. J Clin Invest 2008, 118:3012−3024
51. Watson JE, Kamkar S, James K, Kowbel D, Andaya A, Paris PL, Simko J, Carroll P, McAlhany S, Rowley D, Collins C: Molecular analysis of WFDC1/ps20 gene in prostate cancer. Prostate 2004, 61:192−199
52. Daneman R, Zhou L, Agalliu D, Cahoy JD, Kaushal A, Barres BA: The mouse blood-brain barrier transcriptome: a new resource for understanding the development and function of brain endothelial cells. PLoS One 2010, 5:e13741
53. Roesch K, Jadhav AP, Trimarchi JM, Stadler MB, Roska B, Sun BB, Cepko CL: The transcriptome of retinal Muller glial cells. J Comp Neurol 2008, 509:225−238
54. Rowan S, Chen CM, Young TL, Fisher DE, Cepko CL: Transdifferentiation of the retina into pigmented cells in ocular retardation mice defines a new function of the homeodomain gene Chx10. Development 2004, 131:5139−5152
55. Clauss A, Lilja H, Lundwall A: A locus on human chromosome 20 contains several genes expressing protease inhibitor domains with homology to whey acidic protein. Biochem J 2002, 368:233−242
56. Clauss A, Lilja H, Lundwall A: The evolution of a genetic locus encoding small serine proteinase inhibitors. Biochem Biophys Res Commun 2005, 333:383−389

57. Lundwall A, Clauss A: Genes encoding WFDC- and Kunitz-type protease inhibitor domains: are they related? Biochem Soc Trans 2011, 39:1398−1402
58. Sallenave JM, Shulmann J, Crossley J, Jordana M, Gauldie J: Regulation of secretory leukocyte proteinase inhibitor (SLPI) and elastase-specific inhibitor (ESI/elafin) in human airway epithelial cells by cytokines and neutrophilic enzymes. Am J Respir Cell Mol Biol 1994, 11:733−741
59. Simpson AJ, Wallace WA, Marsden ME, Govan JR, Porteous DJ, Haslett C, Sallenave JM: Adenoviral augmentation of elafin protects the lung against acute injury mediated by activated neutrophils and bacterial infection. J Immunol 2001, 167:1778−1786
60. Zaidi SH, You XM, Ciura S, O'Blenes S, Husain M, Rabinovitch M: Suppressed smooth muscle proliferation and inflammatory cell invasion after arterial injury in elafin-overexpressing mice. J Clin Invest 2000, 105:1687−1695
61. Liu S, Howell P, Ren S, Fodstad O, Zhang G, Samant R, Shevde L, Xi Y, Pannell LK, Riker AI: Expression and functional analysis of the WAP four disulfide core domain 1 gene in human melanoma. Clin Exp Metastasis 2009, 26:739−749
62. Madar S, Brosh R, Buganim Y, Ezra O, Goldstein I, Solomon H, Kogan I, Goldfinger N, Klocker H, Rotter V: Modulated expression of WFDC1 during carcinogenesis and cellular senescence. Carcinogenesis 2009, 30:20−27
63. Orr B, Riddick AC, Stewart GD, Anderson RA, Franco OE, Hayward SW, Thomson AA: Identification of stromally expressed molecules in the prostate by tag-profiling of cancer-associated fibroblasts, normal fibroblasts and fetal prostate. Oncogene 2012, 31:1130−1142
64. Saffroy R, Riou P, Soler G, Azoulay D, Emile JF, Debuire B, Lemoine A: Analysis of alterations of WFDC1, a new putative tumour suppressor gene, in hepatocellular carcinoma. Eur J Hum Genet 2002, 10:239−244
65. De Minicis S, Seki E, Uchinami H, Kluwe J, Zhang Y, Brenner DA, Schwabe RF: Gene expression profiles during hepatic stellate cell activation in culture and in vivo. Gastroenterology 2007, 132:1937−1946
66. Henriksen PA, Hitt M, Xing Z, Wang J, Haslett C, Riemersma RA, Webb DJ, Kotelevtsev YV, Sallenave JM: Adenoviral gene delivery of elafin and secretory leukocyte protease inhibitor attenuates NF-kappa B-dependent inflammatory responses of human endothelial cells and macrophages to atherogenic stimuli. J Immunol 2004, 172:4535−4544